J. Eur. Opt. Society-Rapid Publ. 2023, **19**, 3
© The Author(s), published by EDP Sciences, 2023
https://doi.org/10.1051/jeos/2022017
Available online at: jeos.edpsciences.org

Journal of the European Optical Society-Rapid Publications

RESEARCH ARTICLE OPEN ACCESS

Ultra-broadband and tunable infrared absorber based on VO_2 hybrid multi-layer nanostructure

Junyi Yan[1], Yi Li[1,2,*], Mengdi Zou[1], Jiaqing Zhuang[1], Jincheng Mei[1], Xingping Wang[1], Xin Zhang[1], Yuda Wu[1], Chuang Peng[1], Wenyan Dai[1], Zhen Yuan[1], and Ke Lin[1]

[1] School of Optical-Electrical and Computer Engineering, University of Shanghai for Science and Technology, Shanghai 200093, China
[2] Shanghai Key Laboratory of Modern Optical System, Shanghai 200093, China

Received 20 August 2022 / Accepted 5 December 2022

Abstract. We propose an ultra-broadband near- to mid-infrared (NMIR) tunable absorber based on VO_2 hybrid multi-layer nanostructure by hybrid integration of the upper and the lower parts. The upper part is composed of VO_2 nanocylinder arrays prepared on the front illuminated surface of quartz substrate, and VO_2 square films and $VO_2/SiO_2/VO_2$ square nanopillar arrays prepared on the back surface. The lower part is an array of $SiO_2/Ti/VO_2$ nanopillars on Ti substrate. The effects of different structural parameters and temperature on the absorption spectra were analyzed by the finite-difference time-domain method. An average absorption rate of up to 94.7% and an ultra-wide bandwidth of 6.5 μm were achieved in NMIR 1.5–8 μm. Neither vertical incident light with different polarization angles nor large inclination incident light has a significant effect on the absorption performance of the absorber. The ultra-broadband high absorption performance of this absorber will be widely used in NMIR photodetectors and other new optoelectronic devices.

Keywords: Broadband absorber, Vanadium dioxide, Perfect absorption, Metamaterials, Thermal tuning.

1 Introduction

Metamaterials (MMs) have gained a lot of attention in recent years as a kind of artificially designed and manufactured rational structures with unique physical properties that cannot be achieved by ordinary materials. It consists of special functional unitary structures that are densely embedded in a medium [1]. As an electromagnetic material, its unitary structure can be designed to couple with incident electromagnetic waves and achieve the absorption of the electromagnetic waves [2–4]. Based on these special properties, metamaterials are widely used in sensors [5], high-performance antennas [6], stealth materials [7, 8], and other electromagnetic devices [9, 10]. The application of metamaterial structures in the field of electromagnetic wave absorber has become one of the current research hotspots. Compared with conventional absorbers, metamaterial absorbers have better absorption performance and can be miniaturized and integrated. The size and shape of different material structures in metamaterial absorbers can be adjusted to resonate with specific wavelengths of electromagnetic waves [11]. Therefore, metamaterial structure absorbers targeting the perfect absorption of different wavelengths of electromagnetic waves are emerging [12–16].

* Corresponding author: liyi@usst.edu.cn

In addition to the realization of fixed-band electromagnetic wave absorption, dynamically tunable absorbers have also gained importance. Dynamic tunability of absorbers can be achieved by electrical [17], thermal [18], optical [19], and mechanical tuning [20]. Thermal tuning can be achieved by combining metamaterials with phase change materials. VO_2 has phase change properties that are well suited for application in this study. It can change from the insulating phase to the metallic state at about 68 °C. During the phase change, the electrical conductivity increases by several orders of magnitude with temperature and the process is reversible [21]. The phase transition changes the dielectric environment in the metamaterial structure, which enables the tuning of the absorption spectrum [22]. Cao *et al.* introduced a broadband tunable metamaterial absorber based on different radii of VO_2 rings loaded on the dielectric layer. Based on the insulator-to-metal phase transition characteristics of VO_2 under thermal excitation, the dynamic adjustment of the absorption by the external temperature is achieved [23]. Ban *et al.* propose a convertible metamaterial device with triple-band and broad-band characteristics based on bulk Dirac semimetal (BDS) and VO_2. When VO_2 is in the fully insulating state, the proposed convertible device presents three distinctive absorption peaks in terahertz (THz) range with absorptance >98%. When VO_2 is in the fully metallic state, the

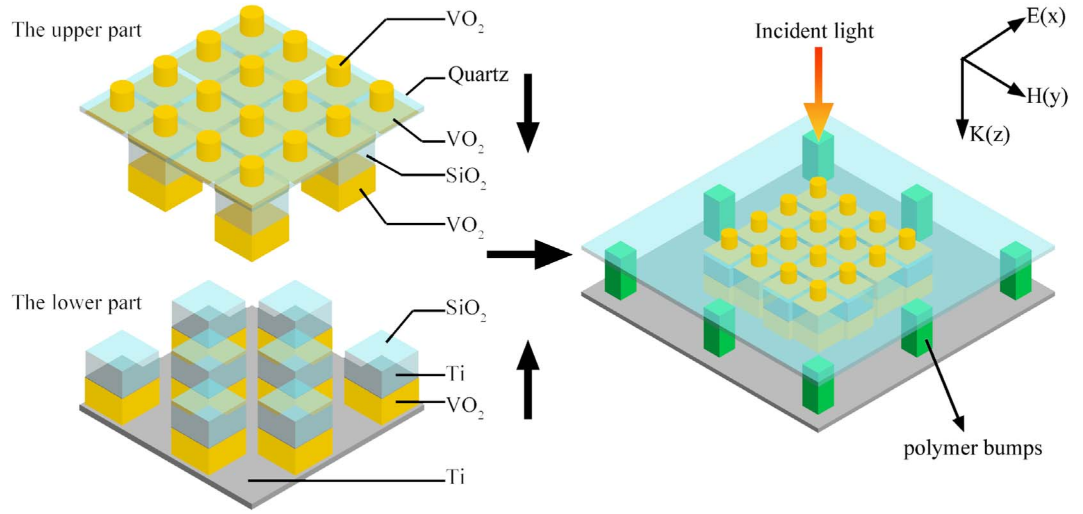

Figure 1. Schematic diagram of absorber by hybrid integration of the upper and lower parts.

convertible device expresses a broad-band absorption [24]. Song *et al.* reported a meta-surface absorber with switchable spectral response. The device is constructed by combining VO_2 and a naturally hyperbolic materials (hexagonal boron nitride, hBN), at different thermal conditions in the same system. The switch between narrow-band near-perfect absorption at ~ 7.2 μm and wide band absorption at 8–12 μm is realized [25].

Although the above absorbers achieve perfect absorption, but it is difficult to achieve the high tunability with both perfect absorption and wide absorption bandwidth. For this reason, we propose an ultra-broadband tunable infrared absorber based on VO_2 hybrid multi-layer nanostructure. The dynamic tunability of different phase states of VO_2 is achieved by the upper and lower parts operating at different temperatures. The absorber achieves efficient absorption rate in the wavelength range of 1.5–8 μm (the average absorption rate exceeds 90%). The absorber can obtain 51.6% of the maximum absorption modulation depth under different operating conditions. In addition, the absorber has polarization-independent properties and achieves high absorption of incident light at large inclination angles in both TE and TM polarization states.

2 Geometry and methods

As shown in Figure 1, the tunable ultra-broadband infrared absorber consists of a hybrid integration of the upper and the lower parts. Figure 2a shows the structure of the unit cell of the absorber. The upper part includes a quartz plate and the nanostructures on its front illuminated and back surface. A VO_2 nanocylinder array is prepared on the front illuminated surface of the quartz substrate. The back surface is the periodically prepared VO_2 square films at positions 1, 2, 3 and 4 of Figure 2a and the SiO_2/VO_2 square nanopillars on the VO_2 square film at positions 2 and 4. The lower part is the $SiO_2/Ti/VO_2$ square nanopillars prepared on the Ti substrate at positions 1 and 3. The upper and lower parts are integrated at a certain interval to form a complete absorber. And after the integration, the center of each structure at the same position in positions 1, 2, 3 and 4 is located in the same line, as shown in Figure 2. For example, the center of the VO_2 nanocylinders on the front illuminated surface of the quartz substrate at positions 2 and 4 and the centers of the VO_2 square films and SiO_2/VO_2 nanopillars on the back surface of the quartz substrate are in the same straight line. Naturally, positions 1 and 3 in Figure 2 are also the same. The absorber with centrosymmetric properties allows it to absorb incident light with different polarization angles [26].

In Figure 2b, the cross section of the unit cell of the absorber with the design structural dimensions indicated is shown. The thicknesses of the quartz substrate and the Ti substrate are d_1 and d_2, respectively. The spacing between the upper and lower parts is Δh. The height of the VO_2 nanocylinder array on the front illuminated surface of the quartz substrate is h, and its radius is r. The thickness and side length of the VO_2 square films are h_1 and L, respectively. L is also the side length of the SiO_2/VO_2 square nanopillars. The height of the VO_2 and SiO_2 square nanopillars in the upper part are h_2 and h_3, respectively. The $SiO_2/Ti/VO_2$ nanopillar prepared on the Ti substrate is similar to the upper part, their side length is L, and their heights are h_2, h_1, h_3, respectively. Figure 2c is a top view of unit cell for the absorber. The period of each cell is p in both x and y directions, which allows the absorber to operate in the NMIR band.

Different temperatures, defined as $T1$ and $T2$, are given to the quartz substrate and Ti substrate by the temperature controller, respectively. Different temperatures allow VO_2 films at the upper part and the lower part to exhibit different properties due to thermally induced phase transition. The reason is that VO_2 has a critical phase transition temperature of 68 °C, where it behaves as an insulator at 20 °C (<68 °C) and changes completely to the metallic phase at 80 °C (>68 °C). We accordingly refer to these two different operating states as VO_2 (I) and VO_2 (M). The optical

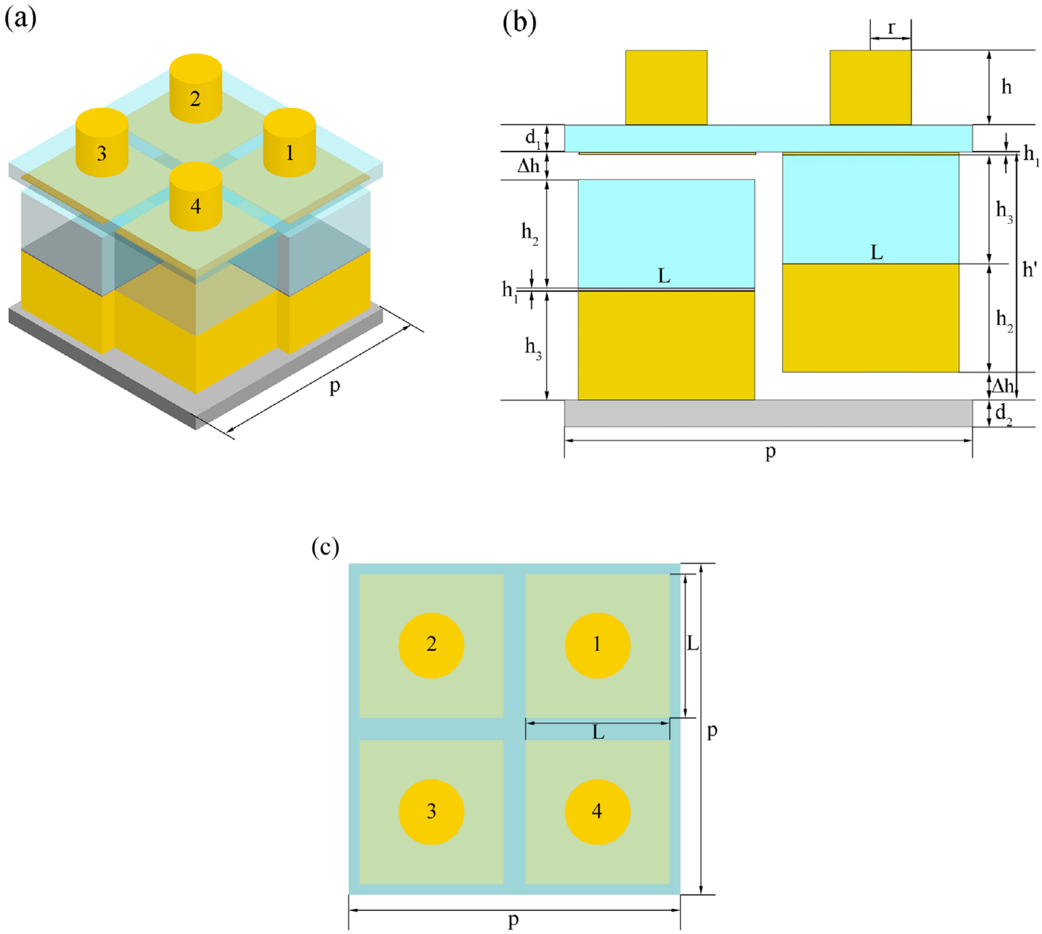

Figure 2. (a) Schematic of the unit cell of the absorber. (b) The cross-sectional view of the absorber. (c) Top view of the unit cell for the absorber.

constants of the VO_2 insulating and metallic phases are taken from the data in refs. [27, 28]. Titanium is a refractory material with low mass density and good stability. In addition, the studies have shown that metamaterials made of titanium (Ti) have broadband absorption properties [29]. Due to its large loss in the imaginary part of the dielectric constant, the absorption loss of light is very high, so it can produce high light absorption in a wide band [30].

As to the fabrication of the proposed structure, the nanopillars and nanocylinder array can be prepared by thin film deposition, photolithography and etching techniques [27]. The polymer bumps with height are fabricated on the edges of the upper part and the lower part to realize the hybrid integration of the upper and the lower parts [31], as shown in Figure 1. Finally, the upper and lower parts are hybridly integrated using interferometric alignment techniques [32], and the center of the VO_2 nanocylinder is aligned with the center of the square nanopillar below it by double side alignment lithography technology [33].

The absorption spectra in the band range of 1.5–8 μm were simulated by Lumerical software using the FDTD solution, data for Ti and SiO_2 were obtained from the PALIK database [34]. The incident light is set as a planar electromagnetic wave incident along the negative direction of the z-axis. When the light is incident positively, periodic boundary conditions are used for the x and y directions. For oblique incidence, the broadband fixed-angle source technique (BFAST) is used. Z direction is always used with a perfectly matched layer (PML) to eliminate the scattered diffraction at the boundary. The reflected spectrum is recorded by a two-dimensional frequency domain power monitor placed behind the incident source, and another power monitor is set below the Ti substrate to record the transmission spectrum. According to energy conservation, the sum of absorption rate $A(\omega)$, reflectance $R(\omega)$ and transmittance $T(\omega)$ is 100%, *i.e.*, $A(\omega) + R(\omega) + T(\omega) = 1$. The absorption rate can be obtained by $A(\omega) = 1 - R(\omega) - T(\omega)$. The electric and magnetic fields are monitored by the frequency profile monitors.

3 Simulation result

3.1 Geometry influence on the absorption

Based on the absorber working principle, the structural parameters determine the absorption performance of the absorber. Firstly, the thicknesses of the two substrates of

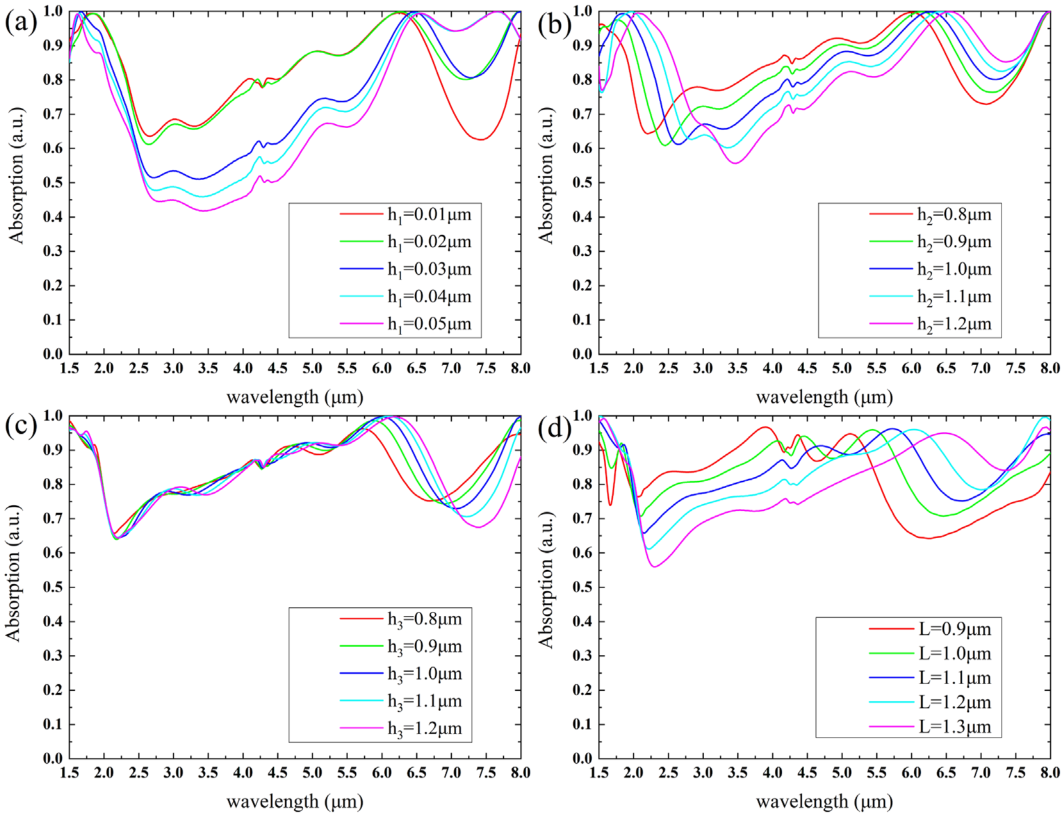

Figure 3. (a) Absorption change with h_1. (b) Absorption change with h_2. (c) Absorption change with h_3. (d) Absorption change with L.

the upper and lower parts need to be determined. The thickness of the substrate does not have much influence on the absorption performance by simulation. Considering the fabrication process, the two substrates need to have a certain strength, so the thicknesses of the quartz substrate and the Ti substrate are set to 200 μm. Through extensive simulations, the initial structural parameters and operating temperatures are set as follows: $L = 1.1$ μm, $h_1 = 0.05$ μm, $h_2 = 1$ μm, $h_3 = 1$ μm, $p = 3$ μm, $\Delta h = 0.1$ μm, $T1 = 80$ °C, $T2 = 20$ °C.

The effect of each geometric parameter on the absorption rate of the absorber without the uppermost VO_2 nanocylinder array was first investigated to obtain the optimal structural parameters. Figure 3a reflects the effect of the thickness h_1 of the VO_2 (M) square film in the upper part and the Ti film in the lower part on the absorption rate. The variation of the absorption curve can be observed to show that the absorption rate is very sensitive to the thickness of the metal film. It can be seen clearly that the absorber gets the best performance when $h_1 = 0.02$ μm and the absorption bandwidth decreases with both increasing and decreasing film thickness. The reason for this phenomenon is that the resonant cavity formed by a too thin film is too small, and when the thickness of the film is too thick, the coupling electric field on its surface is weakened. h_2 is the height of the VO_2 nanopillar in the upper part and the SiO_2 nanopillar in the lower part, and the effect of their height on the absorption performance is shown in Figure 3b. As the height of the VO_2 nanopillar in the upper part increases, the absorption spectrum is red-shifted due to the increase in the height of the metal and the light energy is confined more in the metal [28]. The decrease in absorption rate is related to the thickening of the SiO_2 nanopillar in the lower part that reduces the absorption of light energy by the metal–insulator–metal (MIM) structure below. By simulation, the absorption rate in the wavelength range of 6–8 μm decreases when h_2 is less than 0.8 μm. The absorption curve is optimal when $h_2 = 0.8$ μm.

Figure 3c shows the impact of the height h_3 of the SiO_2 nanopillar in the upper part and the VO_2 nanopillar in the lower part on the absorption spectra. The SiO_2 nanopillars and the VO_2 nanopillars are the intermediate dielectric layer in the MIM structure. There is little change in the absorption spectrum in the 1.5–5.5 μm band with the increase of h_3. In the mid-wave band of 5.5–8 μm, when the height of the intermediate dielectric layer increases, the absorption rate decreases and the resonance absorption peaks are red-shifted. This is because the height of the dielectric layer is the key factor controlling the maximum absorption value and reflection coefficient of the metamaterial absorber [35]. Based on the simulation results in Figure 3c, the highest average absorption rate was found in the wavelength range of 1.5–8 μm for $h_3 = 0.8$ μm. Figure 3d shows the effect of the side length of the nanopillars in the upper and lower part on the absorption performance. When the side length L is small, the air gap

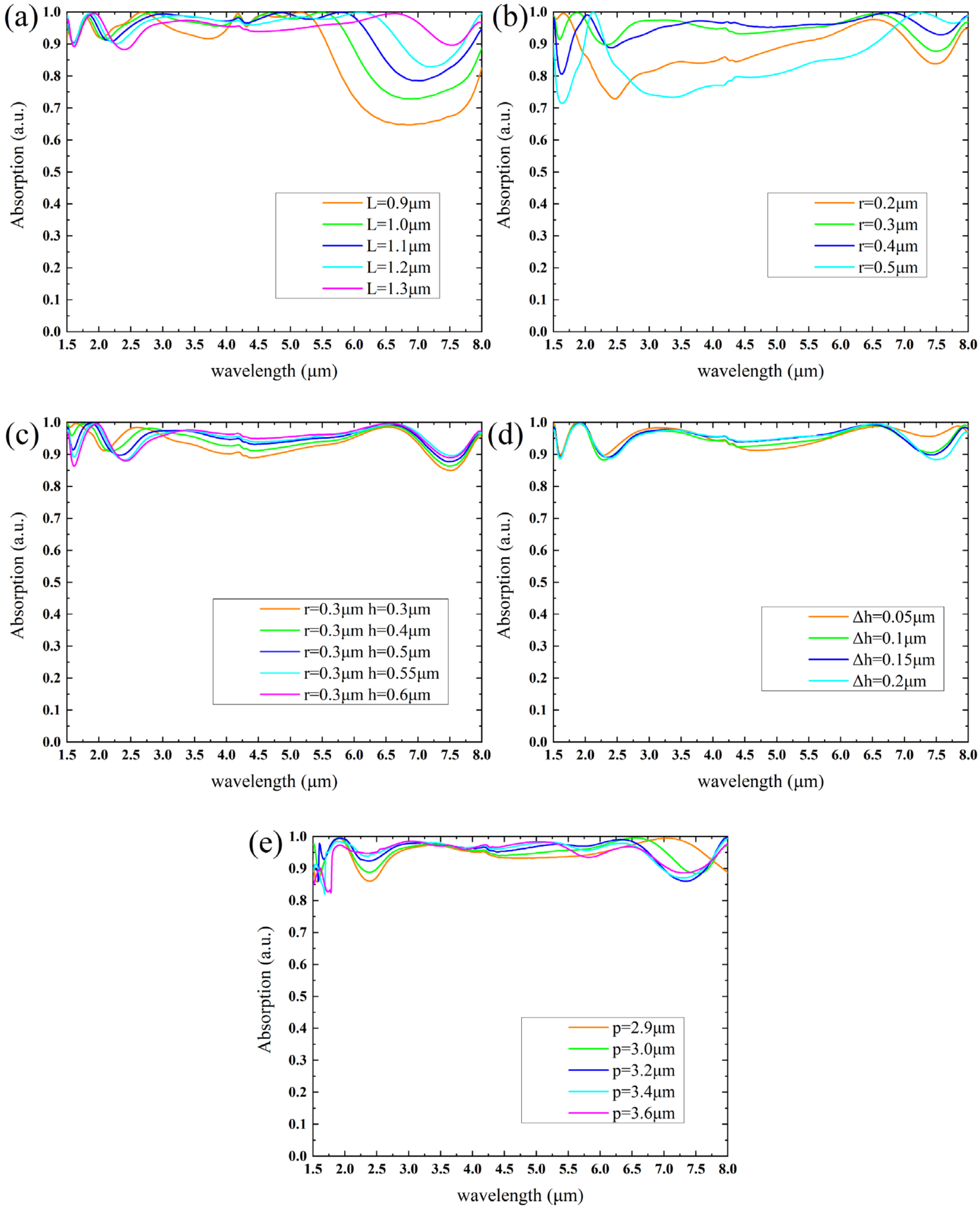

Figure 4. (a) Absorption change with L when the VO_2 nanocylinder array is prepared on the front illuminated surface. (b) Absorption change with the radius of the VO_2 nanocylinder array r. (c) Absorption change with the height of the VO_2 nanocylinder array h. (d) Absorption change with the structural spacing Δh. (e) Absorption change with the variation of individual cycle size p.

between the nanopillars is large and the light cannot be absorbed well. However, when L is too large, the light is reflected out and cannot be absorbed either. $L = 1.3$ μm is chosen as the optimal structure parameter. As can be seen from the four figures in Figure 3, the absorber has a higher absorption rate in the mid-wave band of 6–8 μm without the uppermost VO_2 nanocylinder array.

When the VO_2 nanocylinder array is prepared on the front illuminated surface of the quartz substrate, the overall absorption rate is significantly increased. It is because the uppermost cylindrical array can absorb reflected light that cannot be highly absorbed by the hybrid multi-layer nanostructure. The VO_2 nanocylinders are in metallic state, and the surface plasmon polaritons (SPPs) are generated at their junctions with SiO_2. The metallic cylindrical arrays exhibit strong light absorption due to robust coupling to the waveguide and surface plasmon (SP) modes of the individual columns [36]. Figure 4a illustrates the relationship

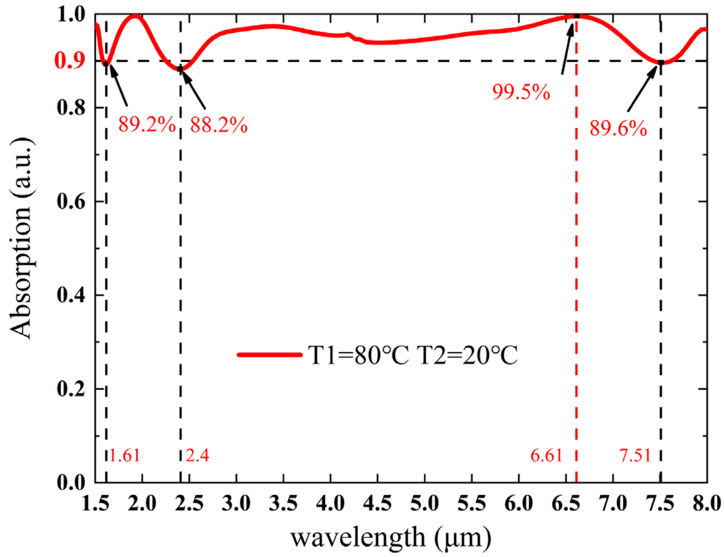

Figure 5. Calculated absorption spectrum.

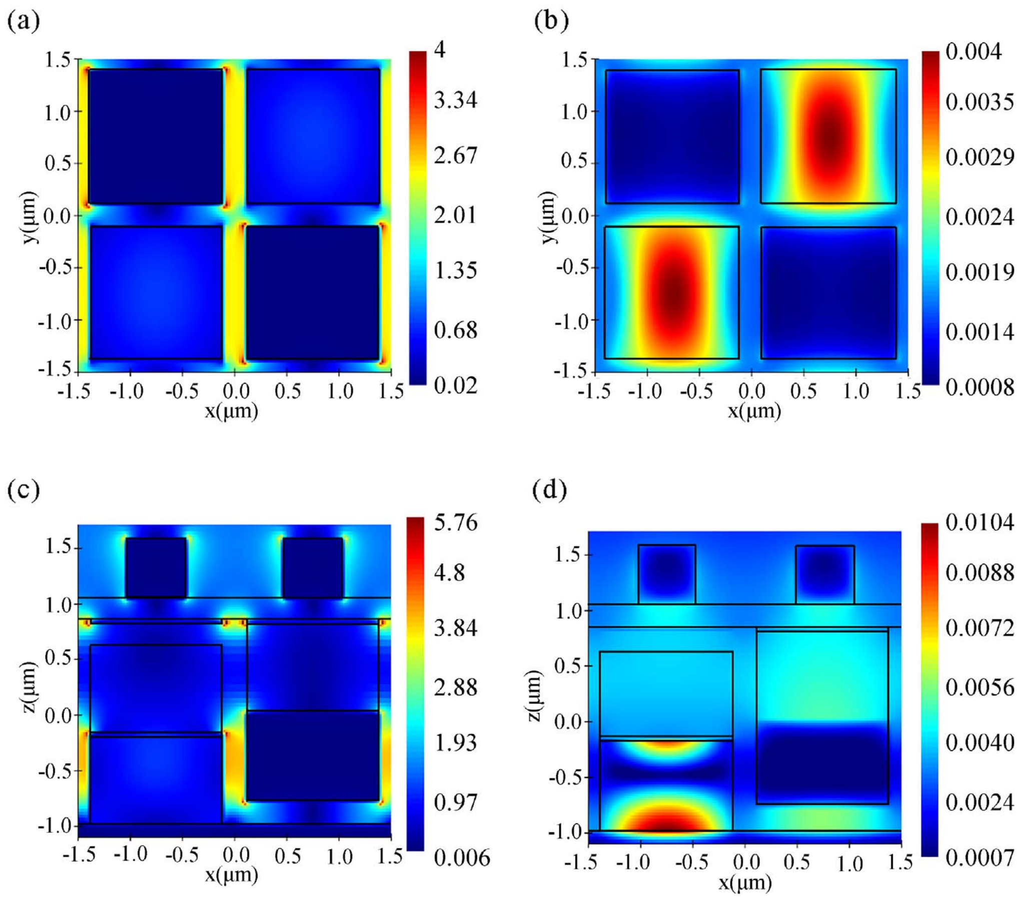

Figure 6. (a) The electric field distribution in XY plane. (b) The magnetic field distribution in XY plane. (c) The electric field distribution in XZ plane. (d) The magnetic field distribution in XZ plane.

between the nanopillar side length and absorption rate when the VO_2 nanocylinder array is prepared in the upper part. It can be found that the absorption rate in the short wavelength band is significantly improved. The high absorption in the entire wavelength band is achieved at L = 1.3 μm. Figure 4b shows the effect of the radius of

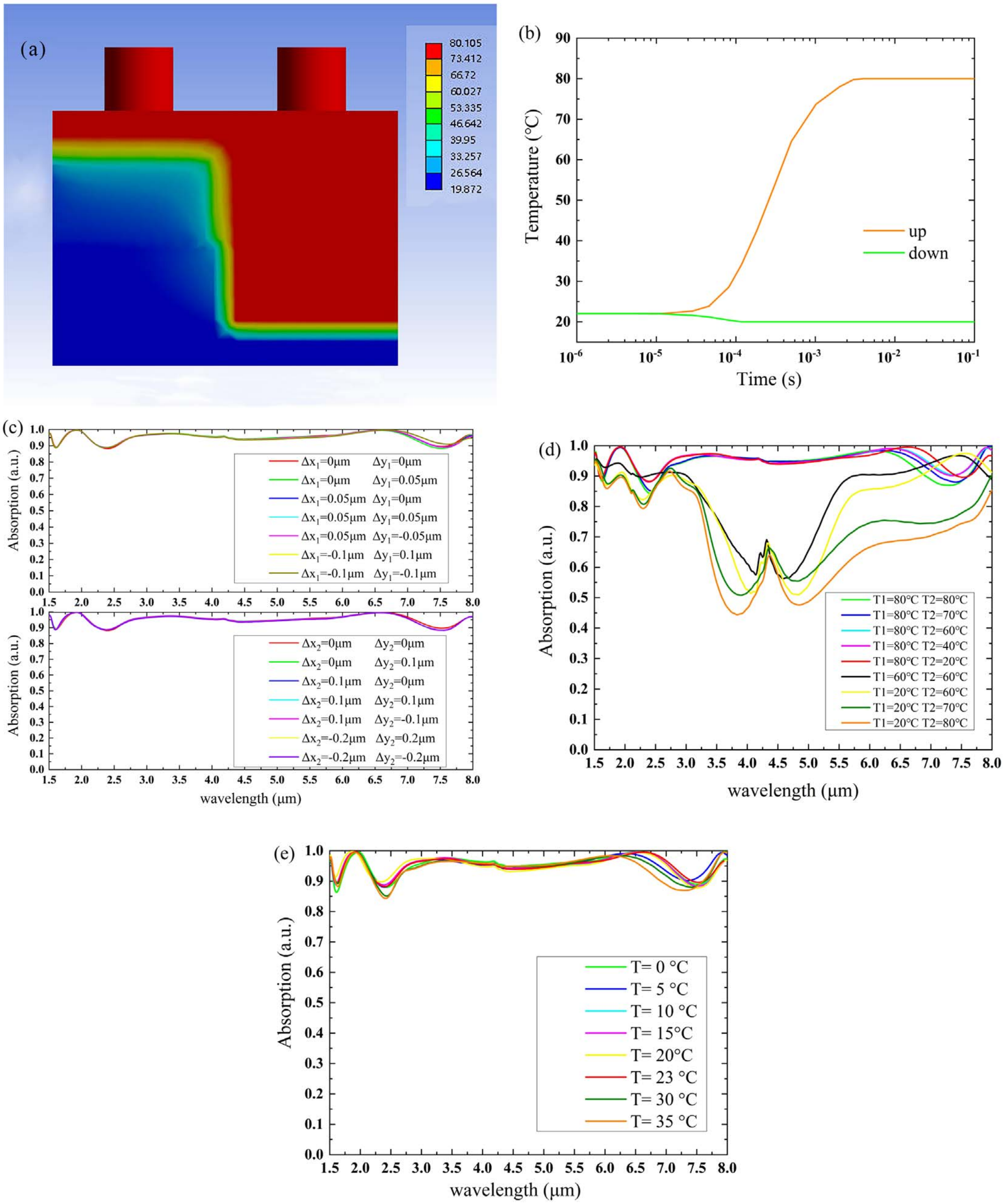

Figure 7. (a) Steady state temperature field distribution of the absorber. (b) Transient temperature change of the absorber. (c) Absorption change with alignment deviation. (d) Absorption change with $T1$ and $T2$. (e) Absorption change with ambient temperature T.

the VO_2 nanocylinder array on the absorption rate. It can be seen that the absorption peaks are red-shifted when r increases. And the absorption rate is very sensitive to r in the wavelength range of 1.5–3.5 μm. Obviously, there is the best absorption performance when $r = 0.3$ μm. From Figure 4c, it is evident that the height of the VO_2 nanocylinder array has a weak effect on the absorption rate. When $h = 0.55$ μm, the absorber has the highest average absorption rate in the wavelength range of 1.5–8 μm. The variation of absorption rate with different structural spacing Δh has little effect, as shown in Figure 4d. The smaller the spacing, the better the absorption performance. Considering the heat conduction of the upper and lower parts and the difficulty of the fabrication process, $\Delta h = 0.2$ μm is chosen as the best value. The change of individual cycle size p also influences the absorption rate of the absorber, as shown in Figure 4e. A small array cycle will make the adjacent gap too small, which is not conducive to light absorption, while a large array cycle will make the distance among the structures too far and the light will reflect out of the absorber. Therefore, $p = 3$ μm is chosen as the optimal array period.

3.2 Absorption performance

From the above simulation results, the optimal structural parameters are obtained: L = 1.3 μm, h_1 = 0.02 μm, h_2 = 0.8 μm, h_3 = 0.8 μm, p = 3 μm, Δh = 0.2 μm. The best absorption spectrum of the proposed broadband tunable absorber based on VO_2 multi-layer nanostructure are illustrated in Figure 5. The temperature of the upper part is controlled at 80 °C, so the VO_2 in the upper part transforms to the metallic state. The VO_2 of the lower part is 20 °C and remains in the insulating state. In the 1.5–8 μm band range, the absorber achieves an average absorption rate of 94.7%, and a peak absorption rate of 99.5% at the wavelength of 6.61 μm.

To study the physical mechanism of the absorber, the electric and magnetic field distributions in the case of vertical positive incidence are simulated. Figures 6a and 6b show the electric field distribution and the magnetic field distribution in the XY direction, and (c) and (d) are the electric and magnetic field distributions in the XZ direction, respectively. The data in Figure 6 were extracted at the wavelength of 6.61 μm. As can be observed from Figures 6a and 6c, the electric field is mainly distributed in the gap of the nanopillar due to the surface plasmon polaritons (SPPs). And the electric field is most intense at the position of VO_2 (M) and the top corner of Ti metal. The SPPs is generated near the metal corner, which couples the energy of light into the gap of the nanopillar and the junction with the surrounding medium. Figures 6b and 6d reflect that the magnetic field is concentrated in the dielectric layers like SiO_2 and VO_2 (I). The propagating surface plasmon (PSP) resonance exists around the interface between VO_2 (I) and Ti substrate. The VO_2 in the insulated state has high dielectric loss, and the absorber binds the electromagnetic wave energy to the center of each unit VO_2 dielectric layer due to the localized surface plasmon (LSP) resonance and converts it into thermal energy, forming a perfect absorption. On the other hand, the magnetic field in the Ti–VO_2 (I)–Ti structure is the strongest, forming a MIM structure. When the incident light penetrates the upper metal, the lower metal acts as a mirror that reflects the LSP excited at the lower metal-dielectric interface, and the LSP between the upper and lower metal-dielectric interface undergo phase extinction interference thereby exciting the resonant cavity mode, leading to a strong absorption of light [37, 38]. Similarly, the uppermost VO_2 (M) cylinder–SiO_2 substrate–VO_2 (M) film and VO_2 (M) film–SiO_2 nanopillar–VO_2 (M) nanopillar also form a MIM structure. The absorption mechanism of the whole absorber is a hybrid mode including SPPs, PSP, LSP and resonant cavity modes, where SPPs primarily dominate the absorption.

3.3 Thermal tuning and tolerance

Since the absorber is integrated by the upper and the lower parts operating at different temperatures, there will be heat diffusion during the heating process. The high temperature of the upper part may affect the working condition of the lower part, so the heat distribution of the absorber is analyzed by ANSYS workbench thermal analysis module

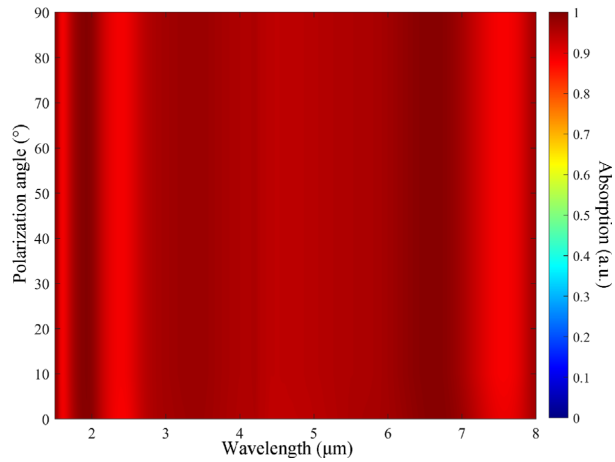

Figure 8. Absorption spectra at different polarization angles.

to exclude the mutual influence of the upper and lower temperatures. There are three main modes of heat transfer between the upper high-temperature part and the lower low-temperature part: heat conduction, heat convection and heat radiation. In the ANSYS simulation, the ambient temperature T is 23 °C and the air convection coefficient is set to 8 W/(m^2·°C), the thermal conductivity and specific heat capacity of VO_2 and SiO_2 at different temperatures are from refs. [39, 40]. Figure 7a shows the simulated steady-state thermal distribution. An external temperature controller is used to heat up the upper quartz substrate at 80 °C and to control the lower Ti substrate at 20 °C. When reached the steady state, the upper and lower parts can maintain their respective temperatures and are not affected by each other, so they can maintain the original operation. Figure 7b shows the transient thermal analysis of the heating process. The upper VO_2/SiO_2/VO_2 nanopillar can be heated to the working temperature of 80 °C in 1 ms, and the lower part can be lowered to 20 °C in 0.1 ms, while VO_2 can undergo phase change in the picosecond range, so the heating and cooling processes of the absorber will not affect the phase change process of VO_2, and the thermal tuning rate of the absorber will not be affected much. After the heating and cooling process, the absorber can also maintain the working temperature stably and achieve stable absorption.

During the fabrication process of hybrid integrating the upper and lower parts, the two parts may have alignment deviations, which also have an impact on the absorption performance of the absorber. Similarly, the alignment deviations in the preparation of the uppermost VO_2 nanocylinder array also have an impact. Figure 7c reflects the absorption spectra for these two alignment deviation cases. Δx_1 and Δy_1 are the deviations of the upper part with respect to the standard positions in the x and y directions, respectively. The deviations of the uppermost VO_2 nanocylinder array with respect to the standard positions in the x and y directions are represented by Δx_2 and Δy_2. From the results, the alignment deviations in the hybrid integration have little effect on the absorptance of the absorber. This proves that the absorber has a good tolerance.

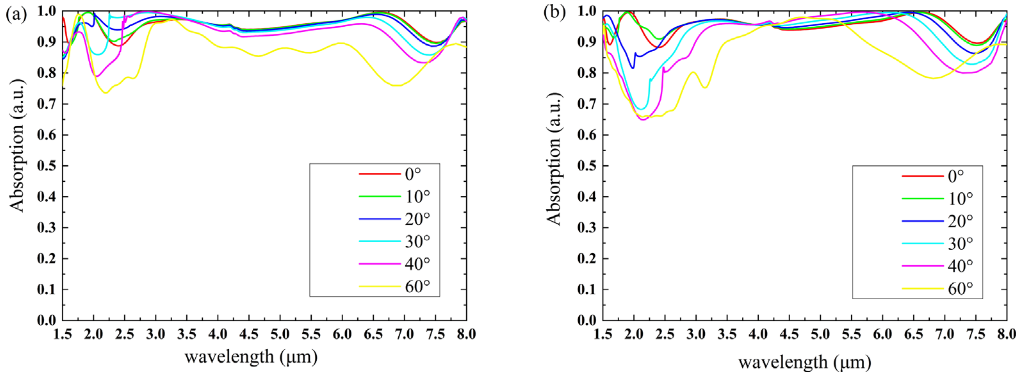

Figure 9. (a) Absorption spectra at different incident angles under TE. (b) Absorption spectra at different incident angles under TM.

Table 1. Comparison of works on the broadband absorbers in the NMIR range in recent years.

Works	Device configuration	ΔB (μm)	$\bar{A}$	FOM (μm)	Tuning method	$h(\lambda) \times \Delta B$ (μm)	Materials involved	Maximum incidence angle
[29]	MIM tri-layer	0.4–2 (1.6)	91.4%	0.82	N/A	N/A	Ti, SiO_2, Ti	50°
[14]	MIM tri-layer	0.1–1.9 (1.8)	93.2%	1.67	N/A	N/A	Ti, W, SiO_2, Au	45°
[43]	Planar layered thin film structures	2–5 (3)	85.3%	2.55	Thermal	1.8	Sapphire, VO_2, PMMA, Au	60°
[44]	L-shaped hybrid nanostructures MIM tri-layer	4.5–6.5 (2)	92.4%	1.84	Thermal	1.54	Au, VO_2, Au	N/A
[28]	Patterned plasmonic metasurface MIM tri-layer	1.6–4.7 (3.1)	93.7%	2.9	Thermal	1.92	Cr, VO_2	60°
[45]	Hybrid nanodisc array MIM tri-layer	0.7–1.8 (1.1)	87.6%	0.96	Thermal	0.7	Au, VO_2, Au	70°
[42]	Nanocolumn array	2–4.8 (2.8)	95.5%	2.67	Thermal	1.4	VO_2, SiO_2, W, Al_2O_3	50°
Our work	Hybrid multi-layer nanostructure	1.5–8 (6.5)	94.7%	6.15	Thermal	3.35	VO_2, SiO_2, Ti	60°

Different operating temperatures also have an effect on the absorption performance of the absorber. Figure 7d shows the variation of absorption spectra for the upper and lower parts of the absorber at different operating temperatures. It can be found that when the temperature of the upper part is kept at high temperature $T1 > 68$ °C and the lower part $T2 < 68$ °C, the different operating temperatures have little effect on the absorption performance of the absorber. This is attributed to the fact that VO_2 films of the upper part and the VO_2 films of the lower part are in metallic and insulating states respectively, the absorber can maintain the original working state. When the temperature of the upper part $T1 < 68$ °C, the VO_2 nanopillar in the upper part changes from the metallic phase to the insulating state, leading to the destruction of the absorption mechanism of the absorber and a decrease in the absorption rate. When $T1 = 80$ °C and $T2 = 20$ °C, the average absorption rate of the absorber in the 1.5–8 μm band range is 94.7%. At $T1 = 20$ °C and $T2 = 80$ °C, the average absorption rate is 44.3%. The absorber can obtain 51.6% of the maximum absorption modulation depth (defined as $h(\lambda) = |A_{\max}(\lambda) - A_{\min}(\lambda)|$). The absorber is dynamically tunable because the thermal phase transition of VO_2 is reversible. Figure 7e shows the effect of the ambient temperature on the absorption spectrum from the absorber when the temperature controller controls $T1 = 80$ °C and $T2 = 20$ °C. It can be seen that the ambient temperature has only a small effect on the performance of the absorber for operating states.

3.4 Optical properties of the absorber at different polarizations and incident angles

Here, we investigate the effect of the polarization and the different angles of incidence on the absorption rate of the absorber. Figure 8 shows the contour plot of the absorption rate evolution when the polarization angle is varied from 0° to 90° for the vertical incidence case. In this study, TM polarization and TE polarization correspond to the polarization angles of 0° and 90°, respectively, *i.e.*, the two cases of electric field parallel or perpendicular to the incident plane. It can be seen that as the polarization angle changes, the absorption rate hardly changes at the same frequency, which indicates that the absorber is polarization-independent. The most obvious reason is that the structure of the absorber is centrosymmetric.

Figure 9 investigates the absorption variation due to different incidence angles under TE polarization and TM polarization. Under TE polarization, the absorption spectra are not affected much when the incident angle gradually increases. In contrast, for TM polarization, when the incident light is at a large angular inclination, some decrease in absorption rate occurs in the 1.5–2.5 μm band range. This is related to the fact that the magnetic field rotates with angle in the case of TM polarization. In conclusion, even for large angular incidence 60°, the absorber still maintains an average absorption rate of more than 80%.

Table 1 shows the comparison of works on the broadband absorbers in the NMIR range in recent years. It is noticeable that the main advantages of our designed absorber are wider absorption bandwidth (1.5–8 μm) and higher overall absorption rate in the NMIR band. A higher figure of merit (FOM) of the absorber $\text{FOM} = \bar{A} \times \Delta B$ can be achieved in this work, where $\bar{A}$ and ΔB are average absorptivity and operation bandwidth [41]. Compared with our previous work [42], the new structural design greatly widens the operation bandwidth of the absorber while maintaining an ultra-high absorption rate. It is reasonable to evaluate the tunability of the absorber by the product of the maximum absorption modulation depth $h(\lambda)$ and the operation bandwidth ΔB as a reference value. The results show that the designed absorber in this work has relatively good tunability, polarization insensitivity and wide-angle absorption characteristics.

4 Conclusion

In conclusion, we propose an ultra-broadband tunable infrared absorber based on VO_2 hybrid multi-layer nanostructure with polarization-independent and wide-angle absorption characteristics. By controlling the temperature of the upper and lower parts, the absorber can achieve tunable ultra-broadband absorption. The physical mechanism of the absorber is elucidated by studying its electromagnetic field distribution and absorption performance comparison. The thermal analysis of the absorber using ANSYS WORKBENCH further verifies the feasibility and tolerance of the structure. The simulation results show that the absorber can achieve an overall absorption rate close to or higher than 90% in the 1.5–8 μm band range, with a high absorption bandwidth of 6.5 μm, which is significantly better than the conventional noble metal metamaterial absorber. The results provide important significance for the research and development of thermoelectric devices that can be widely used in thermal emitters, micro-radiation calorimeters, thermal coolers and infrared detectors.

Conflict of interest

The authors declare no conflicts of interest.

Acknowledgments. This work was supported by the National High Technology Research and Development Program of China (Grant No. 2006AA03Z348); the Foundation for Key Program of Ministry of Education China (Grant No. 207033); the Key Science and Technology Research Project of Shanghai Committee, China (Grant No. 10ZZ94); the Shanghai Talent Leading Plan, China (Grant No. 2011-026).

References

1 Basharin A.A., Kafesaki M., Economou E.N., Soukoulis C.M., Fedotov V.A., Savinov V., Zheludev N.I. (2015) Dielectric metamaterials with toroidal dipolar response, *Phys. Rev. X* **5**, 11.

2 Keiser G.R., Fan K., Zhang X., Averitt R.D. (2013) Towards dynamic, tunable, and nonlinear metamaterials via near field interactions: A review, *J. Infrared Millim. Terahertz Waves* **34**, 709–723.

3 Andryieuski A., Lavrinenko A.V. (2013) Graphene metamaterials based tunable terahertz absorber: Effective surface conductivity approach, *Opt. Express* **21**, 9144–9155.

4 High A.A., Devlin R.C., Dibos A., Polking M., Wild D.S., Perczel J., de Leon N.P., Lukin M.D., Park H. (2015) Visible-frequency hyperbolic metasurface, *Nature* **522**, 192–196.

5 Jiang Y., Liu Z.Y., Matsuhisa N., Qi D.P., Leow W.R., Yang H., Yu J.C., Chen G., Liu Y.Q., Wan C.J., Liu Z.J., Chen X.D. (2018) Auxetic mechanical metamaterials to enhance sensitivity of stretchable strain sensors, *Adv. Mater.* **30**, 8.

6 Wu B.I., Wang W., Pacheco J., Chen X., Grzegorczyk T., Kong J.A. (2005) A study of using metamaterials as antenna substrate to enhance gain, *Prog. Electromagn. Res.* **51**, 295–328.

7 Chandra S., Franklin D., Cozart J., Safaei A., Chanda D. (2018) Adaptive multispectral infrared camouflage, *ACS Photonics* **5**, 4513–4519.

8 Zou J., Zhang J., He Y., Hong Q., Quan C., Zhu Z. (2020) Multiband metamaterial selective absorber for infrared stealth, *Appl. Opt.* **59**, 8768–8772.

9 Guo Y., Cortes C.L., Molesky S., Jacob Z. (2012) Broadband super-Planckian thermal emission from hyperbolic metamaterials, *Appl. Phys. Lett.* **101**, 5.

10 Wang B.X., He Y.H., Lou P.C., Zhu H.X. (2021) Multi-band terahertz superabsorbers based on perforated square-patch metamaterials, *Nanoscale Adv.* **3**, 455–462.

11 Lee B.J., Wang L.P., Zhang Z.M. (2008) Coherent thermal emission by excitation of magnetic polaritons between periodic strips and a metallic film, *Opt. Express* **16**, 11328–11336.

12 Landy N.I., Sajuyigbe S., Mock J.J., Smith D.R., Padilla W.J. (2008) Perfect metamaterial absorber, *Phys. Rev. Lett.* **100**, 4.

13 Motogaito A., Tanaka R., Hiramatsu K. (2021) Fabrication of perfect plasmonic absorbers for blue and near-ultraviolet lights using double-layer wire-grid structures, *J. Eur. Opt. Soc. Rapid Publ.* **17**, 6.

14 Yu P., Yang H., Chen X., Yi Z., Yao W., Chen J., Yi Y., Wu P. (2020) Ultra-wideband solar absorber based on refractory titanium metal, *Renew. Energy* **158**, 227–235.

15 Butun S., Aydin K. (2014) Structurally tunable resonant absorption bands in ultrathin broadband plasmonic absorbers, *Opt. Express* **22**, 19457–19468.

16 Li Voti R. (2018) Optimization of a perfect absorber multilayer structure by genetic algorithms, *J. Eur. Opt. Soc. Rapid Publ.* **14**, 12.

17 Li H., Peng H., Ji C., Lu L., Li Z., Wang J., Wu Z., Jiang Y., Xu J., Liu Z. (2018) Electrically tunable mid-infrared antennas based on VO_2, *J. Mod. Opt.* **65**, 1809–1816.

18 Liang J.R., Li P., Zhou L.W., Guo J.B., Zhao Y.R. (2018) Near-infrared tunable multiple broadband perfect absorber base on VO_2 semi-shell arrays photonic microstructure and gold reflector, *Mater. Res. Express* **5**, 8.

19 Boardman A.D., Grimalsky V.V., Kivshar Y.S., Koshevaya S.V., Lapine M., Litchinitser N.M., Malnev V.N., Noginov M., Rapoport Y.G., Shalaev V.M. (2011) Active and tunable metamaterials, *Laser Photonics Rev.* **5**, 287–307.

20 Pope S.A., Laalej H. (2014) A multi-layer active elastic metamaterial with tuneable and simultaneously negative mass and stiffness, *Smart Mater. Struct.* **23**, 075020.

21 Oka Y., Yao T., Yamamoto N. (1991) Structural phase transition of VO_2(B) to VO_2(A), *J. Mater. Chem. (UK)* **1**, 815–818.

22 Wang S., Kang L., Werner D.H. (2017) Hybrid resonators and highly tunable terahertz metamaterials enabled by vanadium dioxide (VO_2), *Sci. Rep.* **7**, 4326.

23 Cao B., Li Y., Liu X., Fei H., Zhang M., Yang Y. (2020) Switchable broadband metamaterial absorber/reflector based on vanadium dioxide rings, *Appl. Opt.* **59**, 8111–8117.

24 Ban S.H., Meng H.Y., Zhai X., Xue X.X., Lin Q., Li H.J., Wang L.L. (2021) Tunable triple-band and broad-band convertible metamaterial absorber with bulk Dirac semimetal and vanadium dioxide, *J. Phys. D Appl. Phys.* **54**, 6.

25 Song X.L., Liu Z.Z., Scheuer J., Xiang Y.J., Aydin K. (2019) Tunable polaritonic metasurface absorbers in mid-IR based on hexagonal boron nitride and vanadium dioxide layers, *J. Phys. D Appl. Phys.* **52**, 7.

26 Sakurai A., Zhao B., Zhang Z.M. (2014) Resonant frequency and bandwidth of metamaterial emitters and absorbers predicted by an RLC circuit model, *J. Quant. Spectrosc. Radiat. Transf.* **149**, 33–40.

27 Dicken M.J., Aydin K., Pryce I.M., Sweatlock L.A., Boyd E.M., Walavalkar S., Ma J., Atwater H.A. (2009) Frequency tunable near-infrared metamaterials based on VO_2 phase transition, *Opt. Express* **17**, 18330–18339.

28 Lei L., Lou F., Tao K.Y., Huang H.X., Cheng X., Xu P. (2019) Tunable and scalable broadband metamaterial absorber involving VO_2-based phase transition, *Photonics Res.* **7**, 734–741.

29 Liu Z., Liu G., Liu X., Wang Y., Fu G. (2018) Titanium resonators based ultra-broadband perfect light absorber, *Opt. Mater.* **83**, 118–123.

30 Farsinezhad S., Shanavas T., Mahdi N., Askar A.M., Kar P., Sharma H., Shankar K. (2018) Core-shell titanium dioxide-titanium nitride nanotube arrays with near-infrared plasmon resonances, *Nanotechnology* **29**, 154006.

31 Oh K.W., Ahn C.H. (1999) A new flip-chip bonding technique using micromachined conductive polymer bumps, *IEEE Trans. Adv. Packag.* **22**, 586–591.

32 van Soest F.J., van Wolferen H., Hoekstra H., de Ridder R.M., Worhoff K., Lambeck P.V. (2005) Laser interference lithography with highly accurate interferometric alignment, *Jpn. J. Appl. Phys.* **44**, 6568–6570.

33 Wang H.-Y., Wu Z.-H. (2006) Study on the alignment technology process of double-sided lithography on glass substrate, *Semicond. Technol. (China)* **31**, 576–578.

34 Lynch D.W., Hunter W.R. (1997), in: Palik E.D. (ed.), *Handbook of Optical Constants of Solids*, Academic Press, Burlington.

35 Duan G., Schalch J., Zhao X., Zhang J., Averitt R.D., Zhang X. (2018) Analysis of the thickness dependence of metamaterial absorbers at terahertz frequencies, *Opt. Express* **26**, 2242–2251.

36 Zhou P., Zheng G., Chen Y., Xu L., Xian F. (2019) Dynamically tunable perfect absorption based on the phase transition of vanadium dioxide with aluminum hole arrays, *Solid State Commun.* **288**, 48–52.

37 Luo Y., Liang Z., Meng D., Tao J., Liang J., Chen C., Lai J., Qin Y., Lv J., Zhang Y. (2019) Ultra-broadband and high absorbance metamaterial absorber in long wavelength infrared based on hybridization of embedded cavity modes, *Opt. Commun.* **448**, 1–9.

38 Chen H.-T. (2012) Interference theory of metamaterial perfect absorbers, *Opt. Express* **20**, 7165–7172.

39 Oh D.W., Ko C., Ramanathan S., Cahill D.G. (2010) Thermal conductivity and dynamic heat capacity across the metal-insulator transition in thin film VO_2, *Appl. Phys. Lett.* **96**, 3.

40 Hou D., Yuan L.U., Liu Z., Jie H.U.J.M.R. (2017) Temperature rising in VO_2 thin films under irradiation of mid-infrared laser based on external heat source, *Mater. Rev.* **31**, 91–95.

41 Cheng C.-W., Abbas M.N., Chiu C.-W., Lai K.-T., Shih M.-H., Chang Y.-C. (2012) Wide-angle polarization independent infrared broadband absorbers based on metallic multi-sized disk arrays, *Opt. Express* **20**, 10376–10381.

42 Zhao W.Q., Li Y., Tian R., Li J.X., Fan L.N., Zhou J.Z., Liu J., Zhang X., Peng C., Wu Y.D., Zou M.D. (2020) A dynamically temperature tunable broadband infrared absorber with cross square nanocolumn arrays, *Opt. Commun.* **474**, 7.

43 Kocer H., Butun S., Palacios E., Liu Z., Tongay S., Fu D., Wang K., Wu J., Aydin K. (2015) Intensity tunable infrared broadband absorbers based on VO_2 phase transition using planar layered thin films, *Sci. Rep.* **5**, 13384.

44 Moradi T., Hatef A. (2020) Thermal tracing of a highly reconfigurable and wideband infrared heat sensor based on vanadium dioxide, *J. Appl. Phys.* **127**, 9.

45 Zou M.D., Li Y., Zhao W.Q., Zhang X., Wu Y.D., Peng C., Fan L.N., Li J.X., Yan J.Y., Zhuang J.Q., Mei J.C., Wang X.P. (2021) Dynamically tunable perfect absorber based on VO_2-Au hybrid nanodisc array, *Opt. Eng.* **60**, 11.